Monthly Notices of the ROYAL ASTRONOMICAL SOCIETY

MNRAS **526,** 2110–2117 (2023) https://doi.org/10.1093/mnras/stad2897
Advance Access publication 2023 September 28

Particle-in-cell simulations – ion beam instabilities and the generation of Alfvén and whistler waves in low β plasma

H. Che,[1,2]★ A. O. Benz[3,4] and G. P. Zank[1,2]

[1]*Center for Space Plasma and Aeronomic Research (CSPAR), University of Alabama in Huntsville, Huntsville, AL 35805, USA*
[2]*Department of Space Science, University of Alabama in Huntsville, Huntsville, AL 35899, USA*
[3]*University of Applied Sciences and Arts Northwestern Switzerland, CH-5210 Windisch, Switzerland*
[4]*Institute for Particle Physics and Astrophysics, ETH Zürich, CH-8093 Zürich, Switzerland*

Accepted 2023 September 19. Received 2023 September 18; in original form 2023 July 7

ABSTRACT

Ion beam-driven instabilities in a collisionless space plasma with low β, i.e. low plasma and magnetic pressure ratio, are investigated using particle-in-cell (PIC) simulations. Specifically, the effects of different ion drift velocities on the development of Buneman and resonant electromagnetic (EM) right-handed (RH) ion beam instabilities are studied. Our simulations reveal that both instabilities can be driven when the ion beam drift exceeds the theoretical thresholds. The Buneman instability, which is weakly triggered initially, dissipates only a small fraction of the kinetic energy of the ion beam while causing significant electron heating, owing to the small electron-ion mass ratio. However, we find that the ion beam-driven Buneman instability is quenched effectively by the resonant EM RH ion beam instability. Instead, the resonant EM RH ion beam instability dominates when the ion drift velocity is larger than the Alfvén speed, leading to the generation of RH Alfvén waves and RH whistler waves. We find that the intensity of Alfvén waves decreases with decrease of ion beam drift velocity, while the intensity of whistler waves increases. Our results provide new insights into the complex interplay between ion beams and plasma instabilities in low β collisionless space plasmas.

Key words: instabilities – plasmas – turbulence – waves – solar wind.

1 INTRODUCTION

Ion beams are commonly observed in nearly collisionless space and astrophysical plasmas. Understanding the kinetic instabilities and waves that are driven by an ion beam streaming along magnetic fields is an important topic in heliophysics and solar physics. For instance, recent observations made by the *Parker Solar Probe* have shown that ion beams, kinetic instabilities, kinetic waves, and Alfvén waves play important roles in solar wind dynamics (Verniero et al. 2020; Bale et al. 2021; Martinović et al. 2021; Raouafi et al. 2023). Field-aligned ion beams and related instabilities have also been discovered in the upstream region of the Earth's bow shock (Hoppe et al. 1981; Hoppe & Russell 1983; Eastwood et al. 2003; Narita et al. 2003), as well as in interplanetary shocks (Gosling 1983). Furthermore, it has been found that ion beams are associated with particle acceleration in solar flares (Benz & Simnett 1986; Voitenko 1996).

Ion beams can drive a variety of electromagnetic (EM) instabilities and plasma waves, including resonant and non-resonant ion beam instabilities. Each of these instabilities includes right- and left-hand polarizations, which can generate corresponding polarized Alfvén waves (Gary et al. 1984; Gary, Madland & Tsurutani 1985; Gary 1991; Verscharen & Chandran 2013; Verscharen et al. 2013). The ion beam instability is a collective instability, which amplifies the perturbation through wave–particle interactions. Thus, a complete understanding of ion beam instability requires a full kinetic treatment. Extensive studies have been carried out on ion beam instabilities, including those based on a kinetic theory of ion dynamics (Gary et al. 1984, 1985) and hybrid simulations (Daughton, Gary & Winske 1999; Wang & Lin 2003; Ofman et al. 2022). However, these studies have primarily focused on kinetic ion dynamics, while neglecting the kinetic electron dynamics. As a result, they have not fully accounted for electron dynamical-scale instabilities and waves. The ignorance of investigations into electron instabilities and associated electron heating leaves a gap in our understanding of ion beam instabilities.

The ratio of space plasma pressure and magnetic pressure, i.e. $\beta \equiv 8\pi nkT/B^2$, varies in a large range. A large fraction of plasmas is low β plasma, i.e. $\beta \ll 1$. For example, solar corona and the solar wind in the inner heliosphere. *In situ* observations have shown evidence of ion beams, kinetic waves, and Alfvén waves in solar wind, which are likely associated with solar wind heating and acceleration processes (Kasper, Lazarus & Gary 2008; Maruca, Kasper & Bale 2011; Verniero et al. 2020; Bale et al. 2021; Martinović et al. 2021; Raouafi et al. 2023). In this paper, we employ particle-in-cell (PIC) simulations to investigate how both electron and ion dynamics impact the development of ion beam instabilities and the generation of Alfvén waves in low β collisionless plasma, which can be approximated as cold plasma.The conditions to trigger ion beam instabilities are complex and this paper focuses on the EM resonant right-hand (RH) ion beam instability which is common in low β and homogeneous space plasma. It is known that ion beams can also drive electrostatic (ES) Buneman instability (Buneman 1958). The growth

★ E-mail: hc0043@uah.edu

rate of the Buneman instability, which is dominated by electron dynamics, is much faster than the ion dynamics-dominated ion beam instability and can develop intense localized ES fields that trap electrons, leading to strong Landau damping of the kinetic energy of ion beams and electron heating (Che et al. 2013). However, it is not known whether the electron-dynamic-scale Buneman instability can affect the development of the ion-dynamic-scale ion beam instability and the generation of Alfvén waves.

In this study, we investigate these questions for the first time with current-free ion beam PIC simulations for different ion beam velocities ranging from $1v_A$ to $12v_A$ in cold uniform plasma, where v_A is the Alfvén speed. Our findings suggest that the resonant EM RH ion beam instability can effectively quench the Buneman instability from developing further into the non-linear stage. The strong electron heating generated by the Buneman instability does not significantly affect the evolution of the resonant EM RH ion beam instability. As a result, the EM resonant RH ion beam instability can develop well and generate Alfvén waves/whistler waves, similar to the theoretical results dominated solely by the ion dynamics. We find that the intensity of Alfvén waves/whistler waves decreases/increases with a decrease in the ion beam velocity.

2 NUMERICAL MODEL AND PIC SIMULATION SETUP

We use a fully relativistic PIC code p3d (Zeiler et al. 2002) to investigate how an ion beam generates Alfvén waves in a collisionless iso-thermal plasma. The P3D code advances the full set of Maxwell equations with a multigrid field solver that corrects the electric field at controlled intervals. The time-stepping algorithm is an explicit trapezoidal leapfrog. The particles are advanced with the relativistic equations of motion. We initialize the 2.5D current-free PIC ion beam simulations with a uniform magnetic field $\mathbf{B} = B_0\hat{x}$ and electron/ion densities $n_e = n_i = n_0$. The electron velocity distribution function is initialized as a single isotropic Maxwellian, which has no bulk motion. The ions include core ions and beam ions, which are counter-streaming to maintain the current-free condition. The ion velocity distribution function is initialized as a core-beam bi-Maxwellian in the form of

$$f_i = \left(\frac{m_i}{2\pi k}\right)^{3/2}\left[\frac{1-\delta}{T_{c0}^{3/2}}e^{-m_i[v_{i\perp}^2+(v_{ix}-v_{c0})^2]/2kT_{c0}} + \frac{\delta}{T_b^{3/2}}e^{-m_i[v_{i\perp}^2+(v_{ix}-v_b)^2]/2kT_b}\right], \quad (1)$$

where $v_\perp^2 \equiv v_{iy}^2 + v_{iz}^2$, $\delta \equiv n_b/n_0$ is the density ratio between the ion beam density n_b and the core ion n_0, T_{c0}, and T_b are the initial ion temperature of the core and the beam, respectively, v_{c0} is the initial drift velocity of the core ions, and v_b is the initial drift of the beam ions. The drift velocities satisfy $(1-\delta)v_{c0} = -\delta v_b$ to maintain a null current, and the electron temperature $T_e = T_{c0}$.

A total of five ion beam simulations with the same ion beam density ratio $\delta = 0.1$ and different drift velocities were carried out. The five ion beam drifts are $v_b/v_A = 1$, 2, 3, 6, and 12 where $v_A = B_0/(4\pi m_i n_0)^{1/2}$ is the Alfvén speed. All simulations have the same domain size $L_x \times L_y = 200d_i \times 96d_i$ and periodic boundaries in both x and y directions. The grid number $g_x \times g_y = 12\,800 \times 6144$ and the particle number per cell is 100. The mass ratio is $m_i/m_e = 100$. The initial temperature $T_e = T_{c0} = T_b = 0.0625m_i v_A^2$, where the temperature is normalized to $m_i v_A^2$, and the plasma $\beta = 8\pi n_0 T_{c0}/B_0^2 = 0.0625$, closer to the typical plasma $\beta \sim 0.1$ of the solar corona and solar wind near Perihelia. In the following, we will see that plasma with $\beta = 0.1$ can be well-approximated as cold plasma. Thus, the conclusions in this paper can be applied to the cold plasma with $\beta < 0.1$.

All the quantities in this paper are dimensionless and are normalized as follows: length to ion inertial length d_i, time to the ion gyro-frequency $\Omega_i^{-1} = m_i c/eB_0$, density to n_0, velocity to v_A, magnetic field to B_0, and electric field to $E_0 = v_A B_0/c$.

In space collisionless plasma, especially when turbulence is present, a thermal equilibrium is typically difficult to maintain. In non-equilibrium plasmas, the pressure is a tensor in kinetic theory (Che et al. 2018) and defined as follows:

$$\mathbb{P}_{ij} = m\int (v_i - \bar{v}_i)(v_j - \bar{v}_j) f(\mathbf{x}, \mathbf{v}, t) dv^3, \quad (2)$$

where $\bar{v}_i$ and $\bar{v}_j$ are the ith and jth components of the mean velocity of particles. The temperature tensor is then defined as follows:

$$\mathbb{T}_{ij} = \frac{P_{ij}}{\int f(\mathbf{x}, \mathbf{v}, t) dv^3}, \quad (3)$$

the diagonal terms $T_{11} = T_x$, $T_{22} = T_y$ and $T_{33} = T_z$ are the anisotropic temperature components, and the trace of tensor $\mathbb{T}$ is the total thermal energy. Initially, the pressure and temperature are isotropic and hence are scalars.

3 SIMULATION RESULTS

While ion beams can drive the EM ion beam instability and generate Alfvén waves (Gary et al. 1984), their relative drift to the background electrons can also trigger the ES Buneman instability (Buneman 1958). Compared to the EM ion beam instability, the Buneman instability is an electron-driven instability and thus has a much faster growth rate. Consequently, the Buneman instability inevitably occurs when the ion beam drift reaches its threshold. The characteristic of an ES instability is electron heating through a two-step wave–particle interaction process (Che et al. 2009, 2010, 2013). In the first step, the Buneman instability grows and inverse-Landau damping converts the drifting kinetic energy into ES wave; In the second step, electrons are heated by Landau damping that converts wave energy back into electron thermal energy. This process transforms organized bulk kinetic energy into randomized thermal kinetic energy. However, how the Buneman instability affects the development of an EM ion beam instability and the production of Alfvén waves have not been studied previously. In the following section, we first briefly introduce the dispersion relations for the Buneman and ion beam instabilities and then present results from our PIC simulations. We demonstrate how these instabilities compete with each other and contribute to the generation of different waves.

3.1 The triggering of the ES Buneman instability at the beginning of ion beam simulations

In a low β plasma, the ES Buneman instability (Buneman 1958) is anisotropic but the growth rate decreases sharply with the increasing pitch angle (Che 2009; Che et al. 2009). Therefore, in a low β plasma, the one-dimensional general dispersion relation of the Buneman instability along the magnetic field is sufficient. In the core-ion rest frame, the dispersion relation for the ES Buneman instability can be written as follows:

$$1 - \frac{\omega_{pi}^2}{\omega^2} - \frac{\omega_{pe}^2}{(\omega - k_x v_{de})^2} = 0, \quad (4)$$

where v_{de} is the electron drift speed relative to core core ions and $v_{de} = -v_b$.

Table 1. Buneman instability thresholds and the fastest growing modes in the 5 PIC simulations with $\omega_{pe} = 200\Omega_i$ and $v_{te} = 2.5v_A$.

v_b/v_A	1.	2.	3.	6.	12.
v_b/v_{te}	0.4	0.8	1.2	2.4	4.8
$k_{bun}d_i$	NA	NA	67.	33.	17.

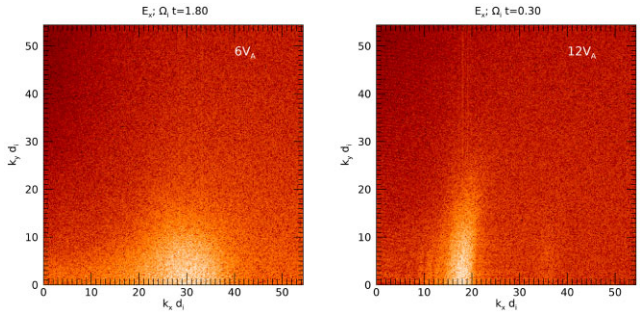

Figure 1. $\delta E_x^2(k_x, k_y)$ for $v_b = 6v_A$ and $v_b = 12v_A$.

The growth rate γ_{bun} and the wave frequency ω_{bun} of the fastest growing mode given by equation (4) are

$$\gamma_{bun} = \frac{\sqrt{3}}{2}(\frac{m_e}{2m_i})^{\frac{1}{3}}\omega_{pe}; \tag{5}$$

$$\omega_{bun} = \frac{1}{2}(\frac{m_e}{2m_i})^{\frac{1}{3}}\omega_{pe}. \tag{6}$$

For a mass ratio of $m_e/m_i = 0.01$, the growth rate of the instability, γ_{bun}, is approximately $0.15\omega_{pe}$, while the corresponding frequency is $\omega_{bun} \sim 0.1\omega_{pe}$ (Che 2009).

The amplitude of the wave vector $\mathbf{k_x}$ of the fastest growing mode of the Buneman instability along the magnetic field is given by equation (4) in Che (2009):

$$k_{x,bun} = \frac{\omega_{pe}}{v_b}. \tag{7}$$

The triggering of the Buneman instability depends on the relative drift speed between ions and electrons and the electron temperature. Previous studies show that the relative drift velocity between the ions and electrons must exceed the background electron thermal speed, v_{te} for the instability to occur (Papadopoulos 1977; Che 2009). However, in practice the Buneman instability can only fully develop when the relative drift is at least two times larger than the electron thermal speed (Papadopoulos 1977; Che 2016).

In Table 1, we list the wavelengths of the fastest growing modes and thresholds for the five simulations with different ion drifts.

The background electron thermal velocity $v_{te} = 2.5v_A$ determines the threshold of the ion beam drift speed for the Buneman instability to trigger. However, for the instability to develop, the drift velocity needs to exceed $2v_{te} = 5v_A$. Therefore while a beam with $v_b = 3v_A$ marginally satisfies the threshold, $v_b = 6v_A$ and $v_b = 12v_A$ are more than twice the electron thermal speed v_{te} and we expect Buneman instability to develop fully in these cases. In Fig. 1, we show the power spectra of $\delta E_x^2(k_x, k_y)$ for simulations with $v_b = 6v_A$ and $v_b = 12v_A$. We can see that Buneman instabilities are triggered at the times $\Omega_i t = 1.8$ and 0.3 for simulations with $v_b = 6v_A$ and $v_b = 12v_A$ respectively, and the corresponding central wavelength $k_x d_i$ is ~33 and 17, which is consistent with the cold plasma limit (Table 1). We do not show the power spectrum of δE_x^2 for the $v_b = 3$ simulation because in this simulation the Buneman instability is weak and is triggered at a much later time when the EM ion beam instability is triggered too, and thus it is difficult to identify the Buneman instability mode. The influence of the Buneman instability in the $v_b = 3$ simulation will be discussed further in Section 3.3.

Table 2. EM resonant ion beam instability ($n_b/n_0 = 0.1$).

v_b/v_A	1	2	3	6	12
v_b/v_{ti}	4	8	12	24	48
$k_{ib}d_i$	1.4	0.7	0.5	0.23	0.12

3.2 The triggering of the resonant EM right-hand ion beam instability

We call an ion beam cold if the beam velocity is significantly larger than the core ion thermal velocity, $v_b \gg v_{ti}$. A cold ion beams can drive the EM ion beam instability. The dispersion relation in the cold plasma limit is

$$\omega_r^2 - k^2c^2 - \frac{\omega_{pi}^2(\omega - k_x v_b)}{\omega - k_x v_b \pm \Omega_i} = 0. \tag{8}$$

Gary et al. (1984) found that an isotropic cold ion beam with sufficiently large v_b can drive a resonant EM RH ion beam instability whose real frequency satisfies the resonant condition near the fastest growing wavenumber

$$\omega_{r,ib} \approx k_x v_b - \Omega_i. \tag{9}$$

The resonant EM RH ion beam instability generates an Alfvén wave satisfying $\omega_r = kv_A$ at long wavelength and makes a transition to a whistler wave as the wave number increases. For beams with densities in the range $0.01 \lesssim n_b/n_0 \lesssim 0.1$, the real frequency is close to the growth rate, i.e. $\omega_r \approx \gamma$. The fastest growing rate can be approximated as follows:

$$\gamma_{ib} \simeq (\frac{n_b}{2n_0})^{1/3}\Omega_i. \tag{10}$$

Equations (9) and (10) for a resonant EM RH ion beam with $\omega_r \approx \gamma$ relates the wavenumber of the fastest growing mode to the density ratio and the ion drift velocity v_b:

$$k_{x,ib} = \frac{[1 + (\frac{n_b}{2n_0})^{\frac{1}{3}}]}{v_b}\Omega_i. \tag{11}$$

In all of the five simulations, the density ratio of the ion beam and the core ions is 0.1, which is within the density range for the resonant EM RH ion beam instability. Thus, the corresponding growth rate γ_{ib} and real wave frequency ω_r for the fastest growing mode are

$$\omega_{r,ib} \approx \gamma_{ib} \sim 0.4\Omega_i. \tag{12}$$

To compare growth rates, we calculated the ratio of the growth rate of the fastest growing mode of the Buneman instability, denoted as γ_{bun}, to that of the ion beam instability, denoted as γ_{ib}. We found that the ratio is approximately equal to the mass ratio, $\gamma_{ib}/\gamma_{bun} \sim m_e/m_i$. As a result, the resonant EM RH ion beam instability grows much slower than the Buneman instability, and reaches its peak at a much later time than the Buneman instability, which occurs at the very beginning of the PIC simulations at $\Omega_i t \sim 0.2$. In our PIC simulations, the mass ratio is $m_i/m_e = 100$, thus the resonant EM RH ion beam instability reaches its peak around $\Omega_i t = 20-30$. The corresponding wavenumbers of the fastest growing mode for the different ion beam drifts are shown in Table 2.

The ion thermal velocity is given by $v_{ti} = 0.25v_A$ for an initial temperature of $T_i = 0.0625$, where $v_{ti} = \sqrt{T_i/m_i}$. As shown in

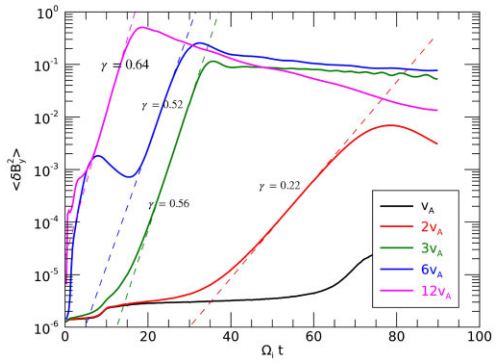

Figure 2. The time evolution of $\langle \delta B_y^2 \rangle$.

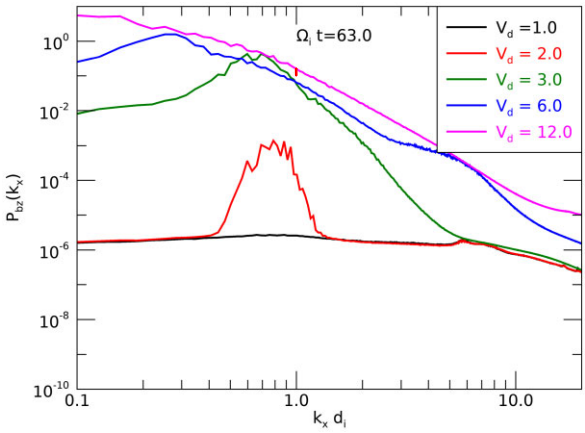

Figure 3. The power-spectra $k_x d_i$ of δB_z^2 at $\Omega_i t = 63$.

Table 2, the ratios of the ion beam drift and the ion thermal velocity v_{ti} in the simulations with drift velocities of $v_b = v_A$ and $2v_A$ are less than 10, while the ratios in the other three simulations are larger than 10. Numerical solutions of the kinetic dispersion relation for the resonant EM RH ion beam instability (Gary et al. 1984) show that a growth rate with $v_b/v_{ti} \sim 10$ is comparable to the peak growth rate, while $v_b = 2v_A$ marginally reaches the threshold and may trigger a resonant EM RH ion beam instability, while $v_b = v_A$ is not large enough to drive the instability.

The resonant EM RH ion beam instability propagating along the magnetic field produces perpendicular magnetic fluctuations δB_y and δB_z. In Fig. 2, we show the time evolution of the mean square of the y-component of the magnetic fluctuations $\langle \delta B_y^2 \rangle = \langle B_y^2 \rangle - \langle B_y \rangle^2$. We can see that the growth rates of δB_y^2 in the simulations with $v_b = 3$, 6, and $12v_A$ are $\gamma = 0.56$, 0.52, and $0.64\Omega_i$, which are close to the growth rate in the cold plasma limit $0.4\Omega_i$. The time at which the instabilities reach their peaks are within the theoretical expected time $\Omega_i t \sim 20$–30. The growth rate of $\langle \delta B_y^2 \rangle$ for the $v_b = 2v_A$ simulation is 0.22, which is ~ 50 per cent of the cold plasma rate 0.4, and the growth rate found for the $v_b = v_A$ simulation is far below the cold plasma rate. The δB_y^2 for $v_b = 2v_A$ peaks around $\Omega_i t \sim 80$, which is also significantly later than the expected time.

We show in Fig. 3 the one-dimensional power-spectra of $\delta B_z^2(k_x)$ along the magnetic field at $\Omega_i t = 63$ for all simulations. The power-spectra peak at $k_x d_i \sim 0.1$, 0.2, and 0.5 for $v_b = 12$, 6, and $3v_A$, respectively, and have similar amplitudes. The wavenumber $k_x d_i$ at which the power-spectra peak are consistent with the cold plasma predictions in Table 2. Despite the power-spectrum for the $v_b = 2v_A$ simulation, peaking at $k_x d_i \sim 0.7$ in agreement with the cold plasma limit in Table 2, the amplitude of the power-spectrum is about two orders of magnitudes lower than those for simulations with higher v_b. The amplitude for $v_b = v_A$ is very small. Therefore, we can conclude that the resonant EM RH ion beam instability is not triggered for $v_b = v_A$ and it is comparatively weak for $v_b = 2v_A$.

3.3 The generation of right-hand polarized Alfvén waves and whistler waves

Gary et al. (1984) have shown that the resonant EM RH ion beam instability can generate RH polarized Alfván waves and whistler waves. Fig. 4 shows the dispersion relations ω_r/Ω_i–kd_i obtained from magnetic fluctuations δB_y propagating along the magnetic field $\mathbf{B}_0 = B_0\hat{x}$. We observe intense Alfván waves in simulations with $v_b = 12v_A$ and $v_b = 6v_A$. The wavenumber increases from $k_x d_i \sim 0.1$ for $v_b = 12v_A$ to $k_x d_i \sim 0.2$ for $v_b = 6v_A$, while the frequency decreases from about $0.1\Omega_i$ to $0.3\Omega_i$. For these two simulations, the whistler wave is relatively stronger for $v_b = 6v_A$, and is nearly invisible for $v_b = 12v_A$ because it is overshadowed by the intensity of the Alfván wave. In simulations with $v_b = 3v_A$ and $2v_A$, the Alfván wave moves to shorter wavelengths and higher frequencies, and becomes too weak to be distinguishable when $v_b = 2v_A$ due to a significant decrease in its relative intensity. Conversely, the whistler wave becomes stronger and dominates near the frequency Ω_i, where the Alfván wave transitions to a whistler wave when $v_b = 3v_A$ and $v_b = 2v_A$, but the absolute wave intensity is reduced by about 100 times. We do not show the dispersion relation for $v_b = v_A$ since no waves are generated in this case.

The resonant EM RH ion beam instability generates RH polarized Alfvén waves and whistler waves, as shown in Fig. 5. Looking along the propagation direction, the circulation of B_y–B_z is clockwise for both waves. Since the ion beam instability trigger time varies, we examine the polarization of B_y–B_z at different times. The left panels display the y-components of the magnetic waves δB_y, where we observe that the waves become less turbulent as the ion beam drift velocity decreases from $v_b = 12v_A$ to $3v_A$, and $2v_A$, but the wave patterns for $v_b = 6v_A$ appear much more turbulent, with a longer wavelength than that for $v_b = 12v_A$. The intensities of both Alfvén and whistler waves are comparable for $v_b = 6v_A$. By comparison, the whistler wave is much weaker in the $v_b = 12v_A$ simulation, and the Alfvén wave is nearly negligible for $v_b = 2v_A$. For $v_b = 3v_A$, although the relative intensities of Alfvén wave and whistler wave are comparable, the absolute strength of the waves is about two orders of magnitude lower than that for the $v_b = 6v_A$ simulation, resulting in a weaker wave coupling. The comparable intensities of Alfvén waves and whistler waves lead to the disparate-scale wave coupling (Che et al. 2017) and the parametric decay results in the sideband antipropagating Alfvén waves at low wavenumber with comparable intensity. The counter propagating Alfvén waves couple with each other and produce a wavepacket with wavelength of $\sim 25d_i$. The disparate coupling between the Alfvén and whistler waves can be seen from the wavefronts shown in the middle panels in Fig. 5 in which the high frequency waves are wrapped inside the wavepacket.

The hodograms of B_y–B_z corresponding to the yellow lines in the left panels are shown in the right panels. In the middle panels, we can see that the waves propagate along the magnetic field in the simulations with $v_b = 2$, 3, and 6 v_A. The wave propagates antiparallel to the magnetic field in the simulation with $v_b = 12v_A$. Along the propagation directions, we can see from the left panels that the rotations of B_y–B_z are all clockwise although the rotation path is entangled for $v_b = 6v_A$ due to the presence of strong turbulence.

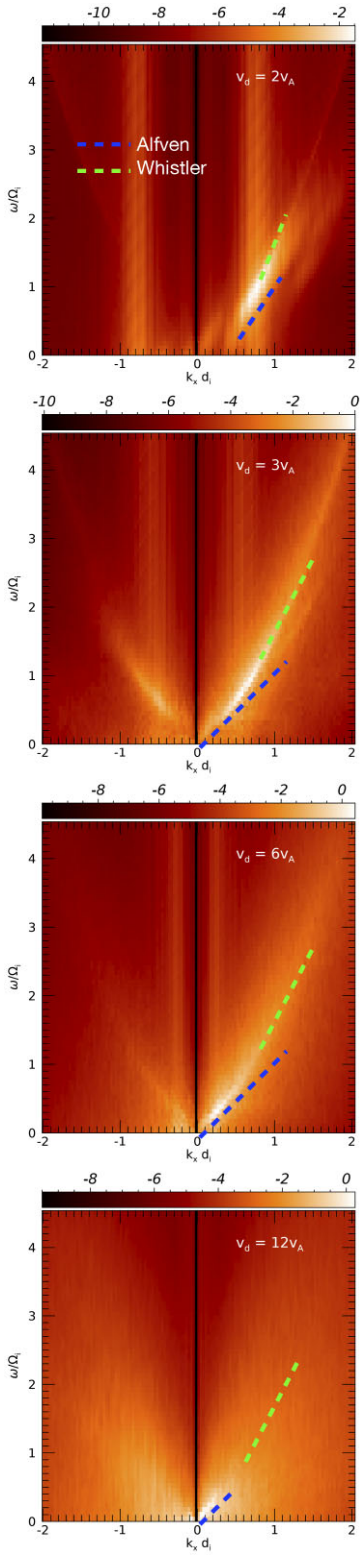

Figure 4. The $\omega_r/\Omega_i - kd_i$ diagrams of parallel propagating low-frequency fluctuations δB_y. The time domain is the whole time duration of the simulations. The power spectra are on a logarithmic scale.

Therefore, the EM resonant ion beam instability is right-handed (RH).

3.4 The transition from Buneman instability to resonant EM RH ion beam instability

Once the Buneman instability is triggered, a fraction of the ion beam kinetic energy is quickly damped and converted into the heating of electrons and ions. As a result, the ion beam drift velocity should decrease due to the loss of the kinetic energy. What we want to know is how much the Buneman instability damps the ion beam energy and affects the onset of the resonant EM RH ion beam instability.

The simulations results shown above illustrate that the resonant EM RH instability is triggered in all simulations except for the $v_b = v_A$ case. In the following, we will discuss why the Buneman instability does not significantly affect the development of the resonant EM RH ion beam instability.

The Buneman instability converts the relative kinetic energy of ions into ES wave energy, leading to the growth of the localized wave potential along the magnetic field and the trapping of electrons whose velocity satisfies $m_e v_e^2/2 < -e\phi$, where ϕ is the ES wave potential that is determined by the loss of the ion beam energy, i.e. $m_i\delta(\Delta v_b)^2/(1-\delta) \sim -e\phi$, where $\delta = n_b/n_0 = 0.1$ and Δv_b is the change of the beam velocity due to the energy loss. The frequency of Buneman wave propagating along magnetic field is $\sim\omega_{pe}$ and thus the parallel electron-wave coupling dominates the plasma heating (Che et al. 2013). As a result, nearly all the damped kinetic energy of the ion beam is converted into suprathermal energy for the trapped electrons, resulting in increase of the parallel temperature of electrons $k\Delta T_{e,\parallel} \sim -e\phi \sim m_i\delta(\Delta v_b)^2/(1-\delta) \sim k\Delta T_{i,\parallel}$. Since the ion–electron mass ratio is large, a small reduction of the ion beam velocity can lead to a large increase of electron temperature. The growth rate of the Buneman instability is $\sim\omega_{pe}$, which determines the heating time-scale. The Buneman instability saturates in a few ion–cyclotron periods. Thus, the electron temperature anisotropy $R_e = \langle(T_{e,\parallel} - T_{e,\perp})/(T_{e,\parallel} + T_{e,\perp})\rangle$ should have a rapid increase. On the other hand, ions initially have a high level of anisotropy due to the contribution from the initial beam drift $T_{i,0} = T_{c0} + m_i\delta v_b^2/(1-\delta) \sim T_{c0} + m_i v_b^2/9$ when we calculate the temperature in the laboratory frame. The ion temperature anisotropy $R_i = \langle(T_{i,\parallel} - T_{i,\perp})/(T_{i,\parallel} + T_{i,\perp})\rangle$ decreases due to the reduction in the ion beam velocity when the Buneman instability is triggered.

In Fig. 6, the left panels show the time evolution of the mean electron and ion temperature anisotropy R_e and R_i while the right panels show the time evolution of mean temperature of electrons and ions. Note that the electron temperature perpendicular to the magnetic field direction x, i.e. T_{ey} and T_{ez} also have a sudden but smaller increase, caused by the scattering of the intensive local electric fields. Both the electron anisotropy R_e for $v_b = 12v_A$ and $6v_A$ have an abrupt increase at the very beginning of the simulations ($\Omega_i t < 5$) when both the ion anisotropy R_i for these two simulations have a slight decrease due to the large mass. However, the ion temperature decrease is approximately equal to the increase of the electron temperature. For $v_b = 12v_A$, the electron temperature increases from the initial temperature $T_{ex} = 0.0625m_i v_A^2$ to $T_{ex} \sim 0.6m_i v_A^2$ and the ion temperature decreases from the initial $T_{ix} \sim 16m_i v_A^2$ to $15.4m_i v_A^2$, then $\Delta T_{ix} \sim \Delta T_{ex} \sim 0.6m_i v_A^2$. Similarly, we find that for $v_b = 6v_A$, $\Delta T_{ix} \sim \Delta T_{ex} \sim 0.2m_i v_A^2$. The temperature changes imply that the decreases of ion beam velocities are about $\delta v_b \sim 0.95v_A$ for

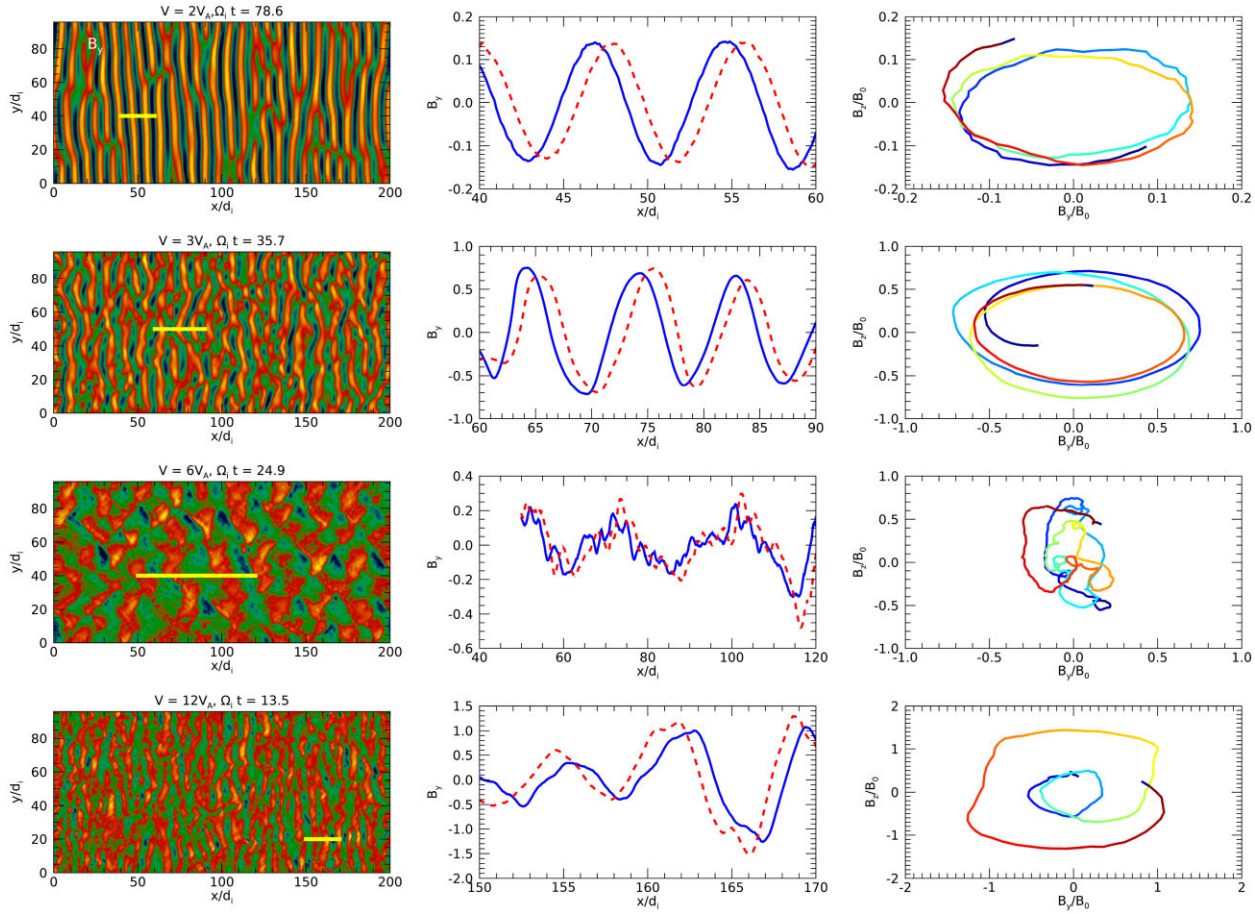

Figure 5. The polarizations of Alfvén waves are shown for the four simulations with $v_b = 2$, 3, 6, and $12v_A$. The left panels display the y-component of magnetic fluctuations δB_y. The middle panels show the waveforms at the cuts marked by yellow lines in the left panels, with solid blue lines representing the times shown in the left panel and red dashed lines representing $\Omega_i t = 0.9$ after those times. This helps visualize the directions in which the waves propagate. The right panels depict the $By-Bz$ trajectory along the yellow lines in the left panels. The track ID colored with blue representing the left end of the line and dark red representing the right end. The waves in the $v_b = 2v_A$, $3v_A$, and $6v_A$ simulations propagate in the x-direction, while the waves in the $v_b = 12v_A$ simulation propagate in the negative x-direction. The polarization of the waves is right-handed.

$v_b = 12v_A$ and $0.45v_A$ for $v_b = 6v_A$, which are small fractions of the kinetic energy of the ion beams and the remaining ion beam drifts are larger enough to trigger the resonant EM RH resonant ion beam instabilities.

The $v_b = 3v_A$ ion beam marginally reaches the threshold of the Buneman instability $v_b \sim v_{te} \sim 2.5v_A$ whereas $v_b = 2v_A$ is smaller than the minimum required velocity. The Buneman instability is not triggered for $v_b = 2v_A$, and is also not visible in the simulation for $v_b = 3v_A$, implying that Buneamn instability is either not triggered or too weak to be detected in the $v_b = 3v_A$ simulation. This can also be seen in the evolution of the electron/ion anisotropy and temperature where no abrupt changes are seen.

Our results indicate that unlike the Buneman instability triggered by electron beams, the ion beam driven Buneman instability is less impacted by electron heating and the Buneman instability can be suppressed quickly once the ion beam instability starts to grow. Eventually the resonant EM RH ion beam instability dominates.

4 CONCLUDING REMARKS

Ion beams can drive the resonant EM RH polarized ion beam instability in low β plasma with nearly isotropic temperature when the ion beam drift v_b is much larger than the ion thermal velocity v_{ti} (Gary et al. 1984). This paper investigates how the electron dynamics impacts the development of the resonant EM RH ion beam instability and the generation of Alfvén waves.

We carried out five PIC ion beam simulations with ion beam velocities $v_b = 1v_A$, $2v_A$, $3v_A$, $6v_A$, and $12v_A$, and a beam density corresponding to 0.1 of the background, consistent with *in situ* space observations of beams. The initial electron thermal velocity is $v_{te} = 2.5v_A$. Of these five PIC ion beam simulations, only those with the ion beam velocities larger than $2.5v_A$ can we expect the Buneman instability to be triggered. However, only for beams with $v_b \geq 2v_{te} = 5v_A$ is the instability expected to develop fully. Indeed, our simulation with a marginally unstable beam velocity of $3v_A$ shows that the Bumeman instability is not visible. Our simulations show that the resonant EM RH ion beam instability can suppress the development of the Buneman instability and significantly reduce the damping of ion beam, and ensure the EM RH ion beam instability can develop and generate the Alfvén waves. The electron heating produced by the Buneman instability does not affect effectively the development of the ion beam instability whose linear growth largely follows the theoretical expectation given by linear kinetic theory (Gary et al. 1984).

As demonstrated by the PIC simulations, the development of the Buneman instability driven by ion beams is very different from the

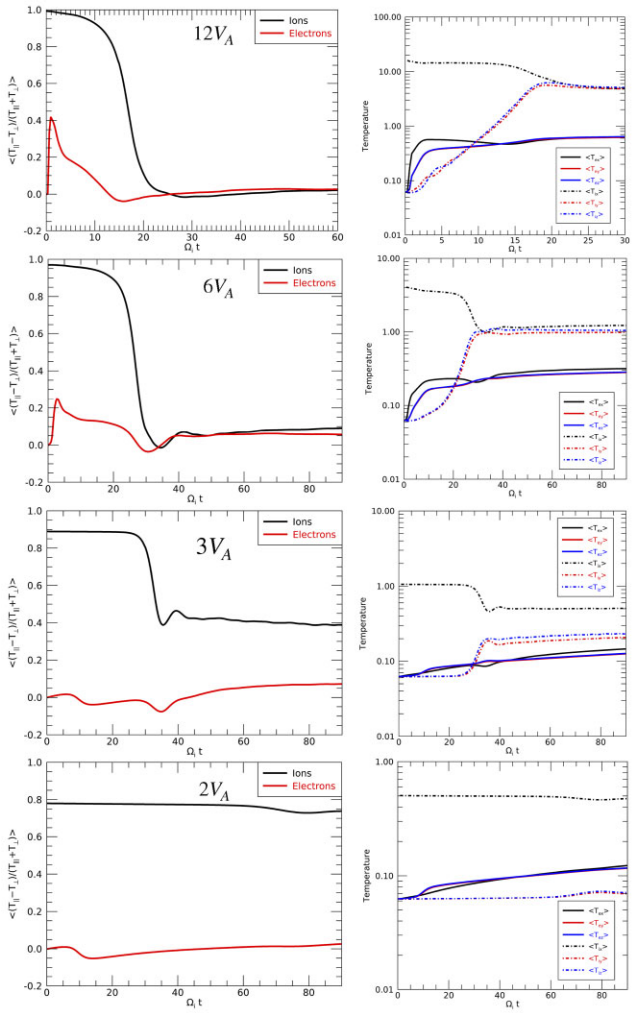

Figure 6. Left panels: the time evolution of the mean temperature anisotropy for both ions and electrons. Right panels: the time evolution of the mean temperature for both ions and electrons.

Buneman instability driven by electron beams. The electron beam-driven Buneman instability grows quickly in a few ion gyro-periods and enters the non-linear stage of the Buneman instability, causing strong dissipation of the kinetic energy of electron beams due to the efficient trapping by the localized intense electric fields, especially for electron beams whose drift are much larger than the electron thermal velocity (Che et al. 2010, 2013). However, the ion beam-driven Buneman instability, even in the case of $v_b = 12v_A$, which is about five times higher than its threshold, the instability grows sharply with a growth rate $\sim 0.15\Omega_{pe}$ initially for about one gyro-period and then is abruptly interrupted as the resonant EM RH ion beam instability grows more steadily with a rate closer to the linear growth rate in the cold plasma limit $\omega_{r,ib} \approx \gamma_{ib} \sim 0.4\Omega_i$. With this slow growth rate, the resonant EM RH ion beam instability peaks at a much later time.

As expected from the linear kinetic theory, the resonant EM RH ion beam instability is triggered in the ion beam PIC simulations for $v_b > v_A$ while the Buneman instability is triggered in ion beam PIC simulations only for $v_b > v_{te} = 2.5v_A$. As a result, the Alfvén waves are generated when the ion beam instability is triggered. However, the intensity of Alfvén waves decreases as the velocity of the ion beam decreases while the whistler wave grows stronger, implying that the generation of whistler waves competes with the generation of Alfvén waves. The underlying physics needs further investigation.

In this paper, we fixed the ion beam density and the isotropic temperature. High ion beam density and velocity can lead to the occurrence of the non-resonant EM RH ion beam instability and left-hand ion beam instabilities (Gary et al. 1984, 1985), and the anisotropy of temperature can lead to the non-resonant firehose and resonant cyclotron instability (Kennel & Scarf 1968). How these instabilities compete with the Buneman instability and generation of Alfvén waves require more studies.

ACKNOWLEDGEMENTS

HC is very grateful to Dr. Y. Yang for his help in analysing the simulations and providing critical comments on the manuscript. HC acknowledges partial support by NSF CAREER 2144324 and and NASA Heliophysics Career award number 80NSSC19K1106. The simulations were supported by the NASA High-End Computing (HEC) Program through the NASA Advanced Supercomputing (NAS) Division at Ames Research Center. We acknowledge the partial support of the NSF EPSCoR RII-Track-1 Cooperative Agreement OIA-2148653.

DATA AVAILABILITY

The simulation data underlying this article will be shared on request.

REFERENCES

Bale S. D. et al., 2021, ApJ, 923, 174
Benz A. O., Simnett G. M., 1986, Nature, 320, 508
Buneman O., 1958, Phys. Rev. Lett., 1, 8
Che H., 2009, PhD thesis, Univ. Maryland, College Park
Che H., 2016, Mod. Phys. Lett. A, 31, 1630018
Che H., Drake J. F., Swisdak M., Yoon P. H., 2009, Phys. Rev. Lett., 102, 145004
Che H., Drake J. F., Swisdak M., Yoon P. H., 2010, Geophys. Res. Lett., 37, 11105
Che H., Drake J. F., Swisdak M., Goldstein M. L., 2013, Phys. Plasmas, 20, 061205
Che H., Goldstein M. L., Diamond P. H., Sagdeev R. Z., 2017, Proc. Natl. Acad. Sci., 114, 1502
Che H., Schiff C., Le G., Dorelli J. C., Giles B. L., Moore T. E., 2018, Phys. Plasmas, 25, 032101
Daughton W., Gary S. P., Winske D., 1999, J. Geophys. Res., 104, 4657
Eastwood J. P., Balogh A., Lucek E. A., Mazelle C., Dandouras I., 2003, Ann. Geophys., 21, 1457
Gary S. P., 1991, Space Sci. Rev., 56, 373
Gary S. P., Foosland D. W., Smith C. W., Lee M. A., Goldstein M. L., 1984, Phys. Fluids, 27, 1852
Gary S. P., Madland C. D., Tsurutani B. T., 1985, Phys. Fluids, 28, 3691
Gosling J. T., 1983, Space Sci. Rev., 34, 113
Hoppe M. M., Russell C. T., 1983, J. Geophys. Res., 88, 2021
Hoppe M. M., Russell C. T., Frank L. A., Eastman T. E., Greenstadt E. W., 1981, J. Geophys. Res., 86, 4471
Kasper J. C., Lazarus A. J., Gary S. P., 2008, Phys. Rev. Lett., 101, 261103
Kennel C. F., Scarf F. L., 1968, J. Geophys. Res., 73, 6149
Martinović M. M., Klein K. G., Ďurovcová T., Alterman B. L., 2021, ApJ, 923, 116
Maruca B. A., Kasper J. C., Bale S. D., 2011, Phys. Rev. Lett., 107, 201101
Narita Y. et al., 2003, Geophys. Res. Lett., 30, 1710
Ofman L., Boardsen S. A., Jian L. K., Verniero J. L., Larson D., 2022, ApJ, 926, 185
Papadopoulos K., 1977, Rev. Geophys. Space Phys., 15, 113
Raouafi N. E. et al., 2023, Space Sci. Rev., 219, 8

Verniero J. L. et al., 2020, ApJS, 248, 5
Verscharen D., Chandran B. D. G., 2013, ApJ, 764, 88
Verscharen D., Bourouaine S., Chandran B. D. G., Maruca B. A., 2013, ApJ, 773, 8
Voitenko Y. M., 1996, Sol. Phys., 168, 219
Wang X. Y., Lin Y., 2003, Phys. Plasmas, 10, 3528
Zeiler A., Biskamp D., Drake J. F., Rogers B. N., Shay M. A., Scholer M., 2002, J. Geophys. Res., 107, 1230

This paper has been typeset from a TEX/LATEX file prepared by the author.